Impact of near-surface wind speed variability on wind erosion in the eastern agro-pastoral transitional zone of Northern China, 1982-2016

Gangfeng Zhang[1,2], Cesar Azorin-Molina[3], Peijun Shi[1,2,4*], Degen Lin[1,5], Jose A. Guijarro[6], Feng Kong[7], Deliang Chen[3]

Surnames (or family names) are underlined

[1] *State Key Laboratory of Earth Surface Processes and Resource Ecology, Beijing Normal University, Beijing 100875, China;*
[2] *Academy of Disaster Reduction and Emergency Management, Ministry of Civil Affairs and Ministry of Education, Beijing Normal University, Beijing 100875, China;*
[3] *Regional Climate Group, Department of Earth Sciences, University of Gothenburg, Gothenburg, 40530, Sweden;*
[4] *Key Laboratory of Environmental Change and Natural Disaster of Ministry of Education, Beijing Normal University, Beijing 100875, China*
[5]*College of Geography and Environmental Sciences, Zhejiang Normal University, Zhejiang 321004, China*
[6]*State Meteorological Agency, Delegation of the Balearic Islands, Palma de Mallorca, Spain;*
[7]*Training Center, China Meteorological Administration. Beijing 100081, China;*

Manuscript submitted to Agricultural and Forest Meteorology

Research Article

14 December 2018

* *Corresponding author address*: Peijun Shi, State Key Laboratory of Earth Surface Processes and Resource Ecology, Beijing Normal University, 19#Xinjiekouwai Street, Haidian District, Beijing 100875, China.

E-mail: spj@bnu.edu.cn

Abstract: Wind erosion in arid and semi-arid areas is an important global environmental issue, and changes in wind speed trends over time play a key role in wind erosion dynamics. In a warming climate, scientists have recently observed a widespread decline in wind speed, termed "stilling". Here, we apply the Revised Wind Erosion Equation Model (RWEQ) to simulate the variability of wind erosion and quantify the impact of wind speed changes on soil degradation dynamics over the eastern agro-pastoral transitional zone of Northern China from 1982 to 2016. Our results show that a significant (i.e., $p<0.05$) decrease (-0.007 m s^{-1} $year^{-1}$) of near-surface wind speed was observed annually, with significant declining trends in spring (-0.010 m s^{-1} $year^{-1}$) and autumn (-0.009 m s^{-1} $year^{-1}$). At the same time, wind erosion simulations reveal a negative trend for the annual soil loss from wind erosion (-6.20 t $hectare^{-2}$ $year^{-1}$, $p<0.05$; affecting 99.8% of the study region), with significant declining trends in all seasons, particularly in spring (-3.49 t $hectare^{-2}$ $year^{-1}$) and autumn (-1.26 $hectare^{-2}$ $year^{-1}$). Further, we isolate the effects of wind variability on wind erosion from 1982 to 2016 by the model variable control method. This shows that wind speed variability strongly weakens wind erosion at -8.14 t $hectare^{-2}$ $year^{-1}$ ($p<0.05$) annually, with the strongest stilling recorded in spring leading to major decreases of wind erosion in spring (-4.77 t $hectare^{-2}$ $year^{-1}$, $p<0.05$). Meanwhile, the weakest stilling in summer had the opposite influence on wind erosion (+0.40 t $hectare^{-2}$ $year^{-1}$, $p<0.10$). To summarize, our findings have shown a significant impact of wind stilling on the decline of soil erosion rates in Northern China.

Keywords: wind erosion; wind stilling; Northern China; Revised Wind Erosion Equation Model

1. Introduction

As the main dynamic force of wind erosion, near-surface winds strongly impact erosion by displacing or removing topsoil from the land surface (Pi et al., 2017; Tegen et al., 1996). Under changing climatic conditions, an observed average near-surface (~10 m height) wind speed trend of -0.140 m s^{-1} dec^{-1} globally has been reported since the 1960s (McVicar et al., 2012). This slowdown of wind speed was first termed "stilling" by Roderick et al. (2007). Many studies have reported similar declines in terrestrial wind speed across the world, especially in the mid-latitudes (Pirazzoli et al., 2003; McVicar et al., 2008; Azorin-Molina et al., 2016; to name but a few). Overall, for China, near-surface wind speed has shown a downward trend in recent decades (e.g., Guo et al., 2011; Lin et al., 2013), with the most significant decline in Northern China (Shi et al., 2015).

The decline of wind speed in recent decades is, in principle, helpful to alleviate soil wind erosion in Northern China, and the rapid warming in the mid-latitudes of the Northern hemisphere (IPCC, 2013), including the agro-pastoral transitional zone of Northern China, may further enhance evaporation. Further, there has been less precipitation in Northern China over the past 50 years, which may have caused more frequent and severe droughts in the agro-pastoral transitional zone of North China (Huang et al., 2017). Drought is not conductive to the growth of surface vegetation as it reduces soil moisture content and weakens soil erosion resistance. Furthermore, anthropogenic activities impact the natural environment (Halpern et al., 2008). Particularly, China's rapid urbanization in recent decades (Bai et al., 2014) has enhanced such activities (i.e., over-farming, land cover changes, etc.), thus making the soil more prone to wind erosion (Zhou et al., 2015).

Wind erosion represents a key environmental issue across the world (Van Pelt et al., 2004; Zhang et al., 2011; Borrelli et al., 2016), especially in arid and semi-arid areas, e.g., southeast Spain (Segovia et al., 2017), northern China (Zhao et al., 2006), Argentinean Pampas (Buschiazzo and Zobeck, 2008), and Egypt (Fryrear et al., 2008). Wind erosion causes the loss of nutrients and organic matter in soil (e.g., Funk and Reuter, 2008; Yan et al., 2013; Segovia et al., 2017), resulting in decreased soil fertility and land productivity (e.g., Holmes et al., 2012; Wang and Shao, 2013; Santra et al., 2017). Comprehensive regional assessments of long-term trends in wind erosion are difficult because observations are often sparse over space and time. Therefore, remote sensing data, which cover a large area, have been successfully used to estimate historical wind erosion (Metternicht et al., 2010; Reiche et al., 2012). Yue et al. (2016) used vegetation cover data from the Pentax A20 digital camera and TM imagery, combined with sediment transport rates from field measurements, showing the slightly increased wind erosion for 1986, 1996, and 2005 in the Mu Us and Yuyang Deserts in North China. Along with remote sensing data, wind erosion models have been applied to estimate spatio-temporal change in wind erosion rates. For instance, Borrelli et al. (2016) applied the Revised Wind Erosion Equation Model (RWEQ) in the arable land of the European Union, reporting the highest values of soil loss in 2001, 2002, and 2004, Alternatively, Zhang et al. (2017) used the Single-Event Wind Erosion Evaluation Program (SWEEP) to estimate annual average wind erosion in Kangbao County, Hebei Province (North China), finding that the SWEEP accurately reproduced a decrease of wind erosion for 2005-2011 when compared against local wind erosion observations.

Wind plays a key role in soil-wind erosion processes (Pi et al., 2017). Furthermore, the warming scenario may intensify aridification in Northern China

(Huang et al., 2016, 2017), including the eastern part of the agro-pastoral transitional zone of Northern China (EANC). Thus, a better understanding of the impact of long-term wind speed changes on the variability of soil erosion is of great importance for many socioeconomic and environmental issues in the agro-pastoral transitional zone of Northern China. However, a lack of long-term wind erosion observations makes this difficult. In view of this, the aims of this study are: (i) to simulate the long-term wind erosion variability by using the RWEQ model in EANC from 1982 to 2016; (ii) to quantify the influence of wind speed variability on wind erosion; and (iii) to provide some new evidence and insights for future soil wind erosion management in Northern China.

2. Study sites

The EANC, located in the southeast of the Mongolian Plateau and northern of the Loess Plateau (108°–124°E, 38°–49°N), is characterized by annual precipitation which varies from 250 to 500 mm; serving as irrigation for agriculture and dry farming over an area of 4.002×105 km^2 (Wang et al., 1999). Within an overall temperate continental climate, its climate varies from semi-humid in the east to arid and semi-arid in the west, mainly controlled by the monsoon and westerly winds. EANC has a complex terrain with plateaus, deserts (e.g., Kubuqi and Ulanbuh), sandlands (e.g., Mu Us and Horqin), and mountains (e.g., Great Khingan), with most of the region (Figure 1) located above 1,000 m a.s.l. (meters above sea level). Typical of arid and semi-arid regions globally, land cover in EANC varies between forest, grassland and barren land with sparse vegetation (Cao et al., 2015). Over recent decades, grassland degradation has been very serious due to the economic interests closely associated with the excessive consumption of grassland resources (Zhai et al.,

2017). The region also has a variety of soil types, including chestnut, aeolian sandy, and gray-brown desert, and most are vulnerable to wind erosion. With strong frequently-occurring winds (Jiang et al., 2010), the risk of wind erosion in EANC is high. Thus, in order to relieve land degradation (i.e., wind erosion) and enhance ecosystem services, nationwide ecological restoration programs have been implemented across EANC in recent years (Cao et al., 2011).

3. Data and methods

3.1. Revised Wind Erosion Equation Model (RWEQ)

In this study, we use the RWEQ model to simulate wind erosion (termed as soil transport) across EANC. This model has been widely applied for regional soil wind erosion prediction and estimation all over the world (e.g., Visser et al., 2005; Borrelli et al., 2017; Pi et al., 2017), and close agreement between simulations and field measurements are found in a number of studies (Buschiazzo and Zobeck, 2008; Youssef et al., 2012). The soil loss (SL) of the area in RWEQ is the total amount of soil transport (Eq. 1, 2, 3), and the full description of the RWEQ formulation can be found in the supplementary material.

$$Qmax=109.8[MF*EF*SCF*K'*C] \quad (1)$$

$$S=150.71(MF*EF*SCF*K'*C)^{-0.3711} \quad (2)$$

$$S_L = \frac{2z}{S^2} Q_{max} e^{-(z/s)^2} \quad (3)$$

where, Qmax is the maximum transfer capacity (in kg m^{-1}); S is the length of key land (in m); SL is soil loss (in kg m^{-2}); Z is the calculated distance of downward wind (in m); MF is the meteorological factor (in kg m^{-1}); EF is the soil erodible factor

(dimensionless); SCF is the soil crust factor (dimensionless); K' is the soil roughness factor (dimensionless); and, C is the vegetation cover factor (dimensionless).

3.2 Data preparation and preprocessing

The RWEQ model requires the following data to model wind erosion: wind speed (at ~10 m, in m s^{-1}), soil moisture (in %), snow depth (in mm), fractional vegetation cover (in %, FVC), and Digital Elevation Model (in m a.s.l., DEM). We also use air temperature (in ºC), precipitation (in mm), and dust storm frequency (in days, over an area bounded between 105ºE - 130ºE and 35ºN - 50ºN) to evaluate climate variability. Table 1 shows the various sources of data used in this study. Figure 1 displays the location of the 71 weather stations, with 25 of them within the EANC and 46 of them covering the surrounding areas; the supporting information in Table S1 describes their characteristics. Station relocations and anemometer height changes (Wan et al., 2010; Azorin-Molina et al., 2014), among many other issues, may cause inhomogeneity in the observed wind speed series. To control quality and homogenize wind speed records, the R package CLIMATOL version 3.1.1 (http://www.climatol.eu/; last accessed 1 November 2018) is used. This robust homogenization protocol has recently been applied in wind studies and a description can be found here: e.g., Azorin-Molina et al., 2018; Shi et al., 2019. Wind speeds are interpolated using standard techniques in the ANUSPLIN package, (Xu and Hutchinson, 2013, http://fennerschool.anu.edu.au/research/; last accessed 1 November 2018).

As the fractional vegetation cover (FVC) data from the Copernicus Global Land Service (CGLS) only covers 1999-2016, we chose the Global Inventory Modeling and Mapping Studies (GIMMS) Normalized Difference Vegetation Index (NDVI) for 1982-1998. Here, the maximum value of the half-month NDVI is used to represent the

monthly NDVI, and then the image binary method (Eq. 4) is applied to calculate the monthly FVC (Gong et al., 2014):

$$FVC = (NDVI\text{-}NDVI_{soil})/(NDVI_{max}\text{-}NDVI_{soil}) \quad (4)$$

Further, a polynomial function is applied between FVC calculated by NDVI and FVC from CGLS during the common period (i.e., 1999-2006), and the FVC is adjusted for 1982-1998. Moreover, to be congruent with the spatial resolution of the FVC, all the monthly data applied in the RWEQ model are resampled into 1 km × 1 km resolution.

3.3 Statistical methods

We calculate wind speed trends in meters per second per year (in m s^{-1} a^{-1}) and soil loss from wind erosion in tons per hectare per year (SLWE, in t ha^{-2} a^{-1}) from 1982 to 2016 using the Sen's slope method (Gilbert, 1987). This involves 5-year moving average series, considering the disturbance of periodic vibration to the original series (Shi et al., 2014). We use the non-parametric correlation coefficient of Mann–Kendall's tau-b (Kendall and Gibbons, 1990) for assessing the statistical significance of linear trends at different timescales, namely annual and seasonal, at three p-level thresholds, (1) significant at $p<0.05$, (2) significant at $p<0.10$, and (3) not significant at $p<0.10$. Moreover, we use a Gaussian low-pass filter of 11 years to determine the decadal changes. We adopt the conventional definition of the four seasons: winter (December–February; DJF), spring (March–May; MAM), summer (June–August; JJA), and autumn (September–November; SON). For determining if and when a change (i.e., break-point year) occurred, we apply the effective and powerful change-point analysis (Gavit et al., 2009). Moreover, we compute the Pearson's correlation coefficient (r) between SLWE and dust storm frequency at the above three p-level thresholds to validate SLWE from RWEQ.

We divide the annual SLWE into six categories according to the Chinese industrial standard of Classification Standard of Soil Erosion (MWRPRC, 2008) as follows: mired wind erosion for 0-2 t ha^{-2}, mild wind erosion for 2-25 t ha^{-2}, moderate wind erosion for 25-50 t ha^{-2}, strong wind erosion for 50-80 t ha^{-2}, very strong wind erosion for 80-150 t ha^{-2}, and fierce wind erosion for more than 150 t ha^{-2}. To isolate the influence of wind stilling on erosion estimates, we use the RWEQ model to compute the experimental soil loss from wind erosion (ESLWE) from 1982 to 2016, while the wind speed is fixed at its 1982 value. The difference between SLWE and ESLWE (SLWED) should reflect the potential influence of wind speed changes on wind erosion in corresponding timescales in every pixel as follows:

$$SLWED = SLWE - ESLWE \quad (5)$$

4. Results

4.1 Near-surface wind speed trends: Observed wind stilling

Figure 2 displays the annual and seasonal variability of wind speed across EANC from 1982 to 2016. Annually, wind speed shows a significant decreasing trend (-0.007 m s^{-1} a^{-1}; $p<0.05$), while a recovery of wind speed is observed for the last decade, as a statistically significant ($p<0.05$) change-point occurred in 2004. Seasonally, a strong negative trend is detected (-0.010 m s^{-1} a^{-1}; $p<0.01$) in spring, and a significant decreasing trend of wind speed is also found in autumn (-0.009 m s^{-1} a^{-1}; $p<0.05$). Further, the magnitude of the decreasing trend is significant in summer (-0.003 m s^{-1} a^{-1}; $p<0.05$). For winter, wind speed exhibits a weak and non-significant ($p>0.10$) decreasing trend (-0.001 m s^{-1} a^{-1}). It is worth noting that there was a recovery of wind

speed in the last couple of decades, with significant change points detected in 2005 (p<0.05) and 2003 (p<0.10), respectively. Meanwhile, spring and autumn experience early significant (p<0.05) recoveries in 1992 and 1998, respectively.

Figure 3 shows the annual and seasonal spatial distribution of wind speed trends across EANC from 1982 to 2016. Annually, declining trends dominate (99.2%; 15.8 % significant at p<0.05), with the strongest declining trends located in the most southern parts; e.g., Khorchin Sandy Land and Hunshadake Sandy Land. The weakest declining trends are also found in the South. Seasonally, this decreasing trend pattern dominates, particularly in autumn (98.6 %; 32.1% significant at p<0.05) and spring (83.8%; 76.4 % significant at p<0.05), with most areas in the south higher than -0.010 m s^{-1} a^{-1}. Meanwhile, the summer exerts the highest percentages of increasing wind speed trends (57.1%; 3.6% significant at p<0.05), mostly occurring over the central and eastern parts of EANC. This is followed by winter (35.1%; 3.1% significant at p<0.05).

4.2. Changes in soil loss from wind erosion

Figure 4 shows the annual and seasonal long-term variability of SLWE over EANC from 1982 to 2016. Annually, the 11-year Gaussian low-pass filter uncovers three phases in the multi-decadal variability of SLWE across EANC: two decreasing periods from 1982-1998 and 2002-2016, and a sudden recovery from 1999 to 2001. The entire annual series shows a declining trend (-6.20 t ha^{-2} a^{-1}; p<0.05). Seasonal statistics reveal a temporal dynamic behavior in the magnitude and statistical significance of the trends throughout the year. Spring exhibits an overall decline of SLWE (-3.49 t ha^{-2} a^{-1}; p<0.01), and a similar sudden recovery detected from 1999-2001 compared to the annual line. For the remaining seasons, SLWE shows

significant decreasing trends, particularly in autumn (-1.26 t ha^{-2} a^{-1}; p<0.05) and summer (-0.85 t ha^{-2} a^{-1}; p<0.05), while winter experiences the decreasing trend to a lesser magnitude (-0.52 t ha^{-2} a^{-1}; p<0.05). More specifically, declining trends for all three seasons are more consistent, and SLWE does not show a sudden recovery compare to spring or annual line.

Figure 5 shows the spatial distribution of average simulated SLWE with the RWEQ across EANC from 1982 to 2016 at annual and seasonal scales. Table 2 summarizes the area and proportion of SLWE. Annually, fierce wind erosion has the highest area of 17*10^4 km^2 (37.1%), followed by moderate (11.88*10^4 km^2, 22.1%), and very strong wind erosion (10.93*10^4 km^2, 20.4%). Strong wind erosion has an area of 8.42*10^4 km^2 (15.7%). Lastly, the proportion of the last two categories is found below 10%, these are mild (4.52*10^4 km^2, 8.4%) and mired (0.9*10^4 km^2, 1.7%) wind erosion. Overall, wind erosion intensity above strong is primarily recorded over the southwestern and eastern part of EANC; e.g., those desert areas with low vegetation cover which are more exposed to strong winds. Meanwhile, wind erosion intensity below strong is mostly present in the southern and northern parts. Seasonally, wind erosion intensity below very strong (34.72*$10^4$$km^2$, 64.7%) dominates in spring. This is mostly located in southern and northern parts. Meanwhile, the fierce and very strong wind erosion are displayed in the western and southwestern parts (18.94*$10^4$$km^2$, 35.3%). Similarly, wind erosion intensity in most areas (>50%) is below moderate for the remaining seasons, whereas wind erosion intensity above strong is recorded in western parts, specifically for summer (2.26*$10^4$$km^2$, 4.2%), autumn (2.58*$10^4$$km^2$, 4.8%), and winter (2.07*$10^4$$km^2$, 3.9%).

Figure 6 shows the annual and seasonal spatial distribution of SLWE trends across

EANC from 1982 to 2016, and Table 3 displays the relative changes in areas (%), reporting positive and negative (and significant) trends. Annually, a consistent decreasing trend of SLWE is detected, with all of the areas showing decreasing trends (99.8% significant at $p<0.05$). The strong magnitude of trends mostly occurs over the northern, central, and southwestern parts (e.g., Khorchin Sandy Land, Hunshadake Sandy Land). Seasonally, there is a similar spatial pattern in spring compared to the annual one, with the highest magnitude of negative trend in SLWE (99.9%; 98.9% significant at $p<0.05$). In contrast, only 0.1% of the area shows increasing trends in SLWE (not significant at $p<0.1$), mainly located in the southern parts. Moreover, the dominated spatial distribution of the decreasing trend of SLWE is detected in summer (99.4%; 95.9% significant at $p<0.05$) and autumn (100%; 100% significant at $p<0.05$), with the markedly decreasing magnitude of trend in SLWE from west to east. Lastly, winter exhibits the highest relative percentage of increasing SLWE (3.85%; 3.2% significant at $p<0.05$) mostly in the western part, and a clear decreasing trend of SLWE is detected in other parts (96.2%; 86.6 % significant at $p<0.05$), particularly in the southwest.

4.3. Validation of RWEQ appropriateness

Accessing the reliability of the simulated SLWE based on the RWEQ is not easy because of a lack of long-term observed wind erosion data. Therefore, we use the observed dust storm frequency data to evaluate the reliability of SLWE simulated by RWEQ. This is because the dust storm particles in the atmosphere are mainly derived from surface wind erosion, which determines the intensity and frequency of the dust storm. Figure 7 displays the annual and seasonal relationship between SLWE and dust storm frequency from 1982 to 2007. Annually, the dust storm frequency is consistent

with the change of SLWE; that is, the dust storm frequency increases with the increase of the SLWE, with a significant correlation coefficient of 0.72 (p<0.05). Seasonally, a statistically significant relationship (p<0.05) is found between dust storm frequency and SLWE in spring (0.67) and summer (0.60). While a less statistically significant relationship (p<0.10) is detected in autumn (0.34), and the relationship between SLWE and dust storm frequency is very weak in winter (0.23, p>0.10)). As a whole, we find a statistically significant relationship between SLWE and dust storm frequency in different timescales, demonstrating that the simulated SLWE change can reveal the real variability of wind erosion across EANC.

4.5. Influence of wind stilling on wind erosion

The potential influence of wind speed changes on wind erosion is reflected by the difference between SLWE and ESLWE, which is shown in Figure 8. Annually, ESLWE is higher than SLWE by 300 t ha^{-2} over the whole period. SLWED significantly decreases at a rate of -8.14 t ha^{-2} a^{-1} (p<0.01). Seasonally, the biggest gap (150 t ha^{-2}) between ESLWE and SLWE is found in spring, followed by summer (100 t ha^{-2}), winter (30 t ha^{-2}), and autumn (20 t ha^{-2}). Moreover, a significant decreasing trend in SLWED of -4.77t ha^{-2} a^{-1} (p<0.05) is detected in spring, followed by winter (-1.42 t ha^{-2} a^{-1}; p<0.05), and autumn (-1.44 t ha^{-2} a^{-1}; p<0.05). Meanwhile, a slighter opposite increasing (p<0.10) trend is found in summer of +0.40 t ha^{-2} a^{-1}.

Figure 9 displays the distribution of SLWED. Annually, SLWED has decreasing trends in most areas (97%; 93.9% significant at p<0.05) over EANC, with the highest magnitude of the decreasing trend found in the central and southwestern parts of the region (e.g., Khorchin Sandy Land and Hunshadake Sandy Land). Meanwhile, weak decreasing trends are found in the northern and southern parts. Seasonally, the highest

percentage of area (95.3%; 90.1% significant at $p<0.05$) with a decreasing trend of SLWED is detected in winter, with the trend shifting from south to north. Spring witnesses the decreasing trends of SLWED in the southwest and northeast (75.6 %; 53.6 % significant at $p<0.05$), and increasing trends are detected in the central part. Moreover, the other seasons exhibit a high percentage of area, with increasing trends of SLWED compared to spring and winter, particularly in summer with more than half of the area (86.3%; 88.6% significant at $p<0.05$), followed by autumn (39.3%; 43.8 % significant at $p<0.05$)，mainly located in central and southern parts.

5. Discussion

The spatio-temporal variability of wind erosion is controlled by different drivers such as vegetation cover changes, precipitation, and wind stilling, among others. In a changing climate, the study of global wind erosion trends is quite complex and uncertainties arise from different sources. Therefore, more detailed regional studies are needed to better understand this phenomenon. For instance, Zhang et al. (2018) estimated that climate change (e.g., wind speed variability) can explain 40.72% of the decline of wind erosion in Inner Mongolia, China from1990 to 2015. In this paper, our results show significant ($p<0.05$) decreasing trends of SLWE at annual and seasonal scales in EANC from 1982 to 2016, which is consistent with the decline of wind erosion reported for the neighboring area, e.g., Xilingol league (Gong et al., 2014) and Ningxia–Inner Mongolia reach of the Yellow River (Du et al., 2017). We also find differences among seasons, with SLWE decline particularly strong in spring and of less magnitude in other seasons. More interestingly, we find a rebound of wind erosion around the year 2001 for annual and spring results. This finding is supported by other studies that report strong spring dust storms occurring in North China in the

early 2000s (e.g., Zhuang et al., 2001; Zhang et al., 2005).

Wind stilling has been confirmed by many recent studies (McVicar et al., 2008; Azorin-Molina et al., 2016; to name but a few). As a whole, annual and seasonal wind speeds show a declining trend across EANC from 1982 to 2016, with varying magnitudes. All these changes in wind speed directly affect wind erosion, thus the reduction of wind erosion rates can be partly attributed to the observed slowdown of surface winds for 1982-2016. Zhang et al. (2017) applied wind tunnel experiments and numerical modeling, finding that the slowdown of surface winds can significantly weaken wind erosion under the same land cover. Moreover, the negligible recovery of wind speed detected in EANC in the last decade is in agreement with some previous studies (Kim and Paik 2015; Azorin-Molina et al., 2018), which also support the low wind erosion in EANC estimated for the same period. Furthermore, we quantify the impacts of surface wind variability on SLWE in our target region, showing that surface wind speed causes the strong decrease of SLWE at annual and seasonal timescales, except for summer when an increase of SLWED is detected; this can partly be explained by the large area of increasing wind speed trends occurring in summer. Positive wind speed trends in summer have been also detected in some other mid-latitude regions such as Spain and Portugal (Azorin-Molina et al., 2014).

Wind erosion is the main particle source of dust storms (Zou and Zhai, 2004; Kurosaki et al., 2011; Avecilla et al., 2017). Therefore, we use dust storm frequency in northern China to verify the simulated soil wind erosion, finding that the average SLWE and dust storm frequency are positively and significantly correlated at annual and seasonal timescales, except for winter. This might be associated with the lowest seasonal wind erosion frequency and intensity in winter and the fact that snow cover inhibits dust storms (Lee and Kim, 2012). In fact, many studies have shown the sharp

reduction of dust storm frequency over northern China in the past few decades (e.g., Song et al., 2016; Wang et al., 2017), which might be related to the dramatic decrease of wind erosion. This is confirmed by the weakened soil wind erosion shown here.

In this study, we only analyze the influence of wind speed changes on wind erosion. However, vegetation is also a key factor contributing to wind erosion (Miao et al., 2012; Mezősi et al., 2015) as it can reduce surface soil exposure and tackle the soil particles. Munson et al. (2011) found that the declining vegetation cover in the Colorado Plateau (United States) strongly increased the wind erosion rates over a 20-year monitoring period. Borrelli et al. (2017) showed that the potential soil loss under permanent bare soil conditions is 22 times higher than the soil loss under vegetation cover in arable lands in the European Union for 2001–2010. Figure 10a displays the increasing trend (+0.14 % a^{-1}, p<0.01) of fractional vegetation cover in the EANC for 1982-2016, in accordance with the vegetation greening observed in northern China during recent decades (Guo et al., 2013; Piao et al., 2015). Nevertheless, a decrease of vegetation cover occurred at the end of the 1990s, which could partly explain the sudden enhanced SLWE around the 2000s. In fact, air temperature (+0.03℃ a^{-1}, p<0.01, Figure.10b) and precipitation (+0.85 mm a^{-1}, p>0.10, Figure.10c) increased very quickly from 1982 to 2016, indicating warming and wetting across EANC. These changes contributed to the growth of vegetation in the region (He et al., 2015; Ren et al., 2018). Further, a full understanding of the factor with the greater influence – i.e., vegetation cover or wind speeds – is needed as increased vegetation can enhance surface roughness/sheltering, thus raising the transport thresholds of wind erosion (Zhang et al., 2017) and weakening surface wind speed (Vautard et al., 2010). Thus, more research is needed to reveal the physical causes behind the unexpected wind erosion decreases of varied vegetation cover and

wind stilling, combined with real observations.

Given the wide decline of global near-surface wind speed highlighted by, e.g., McVicar et al. (2012), and the significant impact of wind slowdown in the decreasing wind erosion rates observed across EANC from 1982-2016, our results suggest that weakened wind speed occurring in other regions of the world can relieve soil degradation in arid and semi-arid land areas; e.g., Sahel and southwest United States. Further research quantifying the impact of wind stilling on wind erosion for other regions is strongly needed. Moreover, the results obtained by modelling wind erosion and dust storm frequency support the application of the same approach for future wind erosion research in other regions. These kind of studies can also help policy-makers take more effective action for ecological conservation (Chen et al., 2017; Zhou et al., 2018) and ecosystem services (Zhao et al., 2015), as well as provide a way to comprehensively assess how wind erosion processes affect the soil organic carbon content (Lugato et al., 2016) and their economic losses (Riksen & De Graaff, 2001).

6. Conclusion

To summarize, the main findings are as follows:

1. Wind stilling was observed in EANC, as the annual average wind speed statistically declined (-0.007 m s^{-1} a^{-1}, $p<0.05$) from 1982 to 2016, displaying a noticeable decreasing seasonal pattern, with the highest negative trend in spring (-0.010 m s^{-1} a^{-1}, $p<0.05$), and the lowest, not significant one in summer (-0.001 m s^{-1} a^{-1}, $p>0.10$).

2. The simulations show that areas of wind erosion intensity above strong dominated EANC by occupying 69.5% of the territory. The annual simulated SLWE exhibits a significant declining trend (-6.2 t ha^{-2} a^{-1}, $p<0.05$) from 1982 to 2016, with 99.8% of EANC showing a significant ($p<0.05$) weakening. Seasonally, a negative

trend of simulated SLWE was found for all seasons, being the highest in spring (-3.49 t ha^{-2} a^{-1}) and lowest in winter (-0.52 t ha^{-2} a^{-1}).

3. Statistical analyses also estimate the direct impact of observed wind speed variability on soil erosion, finding that wind stilling strongly weakened wind erosion rates across EANC from 1982 to 2016. SLWE due to wind speed variability was quantified at rate of -8.14 t ha^{-2} a^{-1} (p<0.05). Seasonally, the strongest stilling recorded in spring led to the major declines in SLWE (-4.77 t ha^{-2} a^{-1}, p<0.05), whereas the weakest stilling found in summer had the opposite influence with a slight increase of SLWE rates (+0.40 t ha^{-2} a^{-1}, p<0.10).

Acknowledgements

This study is supported by the National Natural Science Foundation of China (Grant No.41621061, 41271286), the National Key Research and Development Program–Global Change and Mitigation Project (Grant No.2016YFA0602404), and the European Union's Horizon 2020 research and innovation program under the Marie Skłodowska-Curie grant agreement No. 703733 (STILLING project). This work has been also supported by the Swedish Research Council (VR 2017-03780) and the Swedish Foundation for International Cooperation in Research and Higher Education (STINT CH2015-6226). The authors wish to acknowledge the anonymous reviewers for their detailed and helpful comments to the original manuscript.

Supporting information

Table S1 Description of meteorological stations in the EANC.

The full description of the RWEQ formulation.

References

Avecilla, F., Panebianco, J. E., & Buschiazzo, D. E. (2017). Meteorological conditions during dust (PM10) emission from a tilled loam soil: Identifying variables and thresholds. Agric. For. Meteorol. 244–245(May), 21–32. https://doi.org/10.1016/j.agrformet.2017.05.016.

Azorin-Molina, C., Vicente-Serrano, S. M., Mcvicar, T. R., Jerez, S., Sanchez-Lorenzo, A., López-Moreno, J. I., … Espírito-Santo, F. (2014). Homogenization and assessment of observed near-surface wind speed trends over Spain and Portugal, 1961-2011. J. Clim. 27(10), 3692–3712. https://doi.org/10.1175/JCLI-D-13-00652.1.

Azorin-Molina, C., Guijarro, J. A., McVicar, T. R., Vicente-Serrano, S. M., Chen, D., Jerez, S., & Espírito-Santo, F. (2016). Trends of daily peak wind gusts in Spain and Portugal, 1961–2014. J. Geophys. Res. D: Atmos. 121(3), 1059–1078. https://doi.org/10.1002/2015JD024485.

Azorin-Molina, C., Rehman, S., Guijarro, J. A., McVicar, T. R., Minola, L., Chen, D., & Vicente-Serrano, S. M. (2018). Recent trends in wind speed across Saudi Arabia, 1978–2013: a break in the stilling. Int. J. Clim. 38, e966–e984. https://doi.org/10.1002/joc.5423.

Bai, X., Shi, P., & Liu, Y. (2014). Realizing China's urban dream. Nature. 509(7499), 158–160. https://doi.org/10.1038/509158a.

Borrelli, P., Panagos, P., Ballabio, C., Lugato, E., Weynants, M., & Montanarella, L.

(2016). Towards a Pan-European Assessment of Land Susceptibility To Wind Erosion. L. Degrad. Dev. 27(4), 1093–1105. https://doi.org/10.1002/ldr.2318.

Borrelli, P., Lugato, E., Montanarella, L., & Panagos, P. (2017). A New Assessment of Soil Loss Due to Wind Erosion in European Agricultural Soils Using a Quantitative Spatially Distributed Modelling Approach. L. Degrad. Dev. 28(1), 335–344. https://doi.org/10.1002/ldr.2588.

Buschiazzo, D. E., & Zobeck, T. M. (2008). Validation of WEQ, RWEQ and WEPS wind erosion for different arable land management systems in the Argentinean Pampas. Earth Surf. Process. Landforms. 33(12), 1839-1850. https://doi.org/10.1002/esp.1738.

Cao, Q., Yu, D., Georgescu, M., Han, Z., & Wu, J. (2015). Impacts of land use and land cover change on regional climate: A case study in the agro-pastoral transitional zone of China. Environ. Res. Lett. 10(12), 124025. https://doi.org/10.1088/1748-9326/10/12/124025.

Cao, S., Chen, L., Shankman, D., Wang, C., Wang, X., & Zhang, H. (2011). Excessive reliance on afforestation in China's arid and semi-arid regions: Lessons in ecological restoration. Earth-Science Rev. 104(4), 240–245. https://doi.org/10.1016/j.earscirev.2010.11.002.

Chen, H., Shao, L., Zhao, M., Zhang, X., & Zhang, D. (2017). Grassland conservation programs, vegetation rehabilitation and spatial dependency in Inner Mongolia, China. Land use policy. 64, 429–439. https://doi.org/10.1016/j.landusepol.2017.03.018.

Du, H., Wang, T., & Xue, X. (2017). Potential wind erosion rate response to climate and land-use changes in the watershed of the Ningxia–Inner Mongolia reach of the Yellow River, China, 1986–2013. Earth Surf. Process. Landforms. 42(13),

1923–1937. https://doi.org/10.1002/esp.4146.

Fryrear, D.W., Wassif, M.M., Tadrus, S.E., Ali, A.A., 2008. Dust measurements in the

Funk, R., Reuter, H. I., Hoffmann, C., Engel, W., & Öttl, D. (2008). Effect of moisture on fine dust emission from tillage operations on agricultural soils. Earth Surf. Process. Landforms. 33(12), 1851-1863. https://doi.org/: 10.1002/esp.1737.

Gavit, P., Tholmer, R., & Baddour, Y. (2009). Use of change-point analysis for process monitoring and control. A better method for trend analysis than CUSUM and control charts. BioPharm International 22 (8). http://www.biopharminternational.com/use-changepoint-analysis-process-monitoring-and-control?id=&sk=&date=&pageID=5 (accessed 1 June 2018).

Gilbert RO. 1987. 6.5 Sen's nonparametric estimator of slope. In Statistical Methods for Environmental Pollution Monitoring. Van Nostrand Reinhold Company Inc: New York, 217–219. ISBN: 0-442-23050-8.

Gong, G., Liu, J., & Shao, Q. (2014). Wind erosion in xilingol league, inner mongolia since the 1990s using the revised wind erosion equation.Progress in Geography. 33(6), 825-834. (in Chinese with an English abstract).

Guo, H., Xu, M., & Hu, Q. (2011). Changes in near-surface wind speed in China: 1969-2005. Int. J. Climatol. 31(3), 349–358. https://doi.org/10.1002/joc.2091.

Guo, Z. Di, Hu, H. F., Li, P., Li, N. Y., & Fang, J. Y. (2013). Spatio-temporal changes in biomass carbon sinks in China's forests from 1977 to 2008. Sci. China, Ser. C: Life Sci. 56(7), 661–671. https://doi.org/10.1007/s11427-013-4492-2.

Halpern, B. S., Walbridge, S., Selkoe, K. A., Kappel, C. V., Micheli, F., D'agrosa, C., ... & Fujita, R. (2008). A global map of human impact on marine ecosystems. Science. 319(5865), 948-952.https://doi.org/10.1126/science.1149345.

He, B., Chen, A., Wang, H., & Wang, Q. (2015). Dynamic response of

524 satellite-derived vegetation growth to climate change in the three north shelter
525 forest region in China. Remote Sens. 7(8), 9998–10016.
526 https://doi.org/10.3390/rs70809998.
527 Holmes, P. J., Thomas, D. S. G., Bateman, M. D., Wiggs, G. F. S., & Rabumbulu, M.
528 (2012). Evidence for land degradation from aeolian sediment in the west-central
529 free state province, South Africa. L. Degrad. Dev. 23(6), 601–610.
530 https://doi.org/10.1002/ldr.2177.
531 Huang, J., Yu, H., Guan, X., Wang, G., & Guo, R. (2016). Accelerated dryland
532 expansion under climate change. Nat. Clim. Chang. 6(2), 166–171.
533 https://doi.org/10.1038/nclimate2837.
534 Huang, J., Yu, H., Dai, A., Wei, Y., & Kang, L. (2017). Drylands face potential threat
535 under 2 °c global warming target. Nat. Clim. Chang. 7(6), 417–422.
536 https://doi.org/10.1038/nclimate3275.
537 IPCC. (2013). Climate Change 2013: The Physical Science Basis. Contribution of
538 Working Group I to the Fifth Assessment Report of the Intergovernmental Panel
539 on Climate Change, Cambridge: Cambridge University Press.
540 Jiang, Y., Luo, Y., Zhao, Z., & Tao, S. (2010). Changes in wind speed over China
541 during 1956-2004. Theor. Appl. Climatol. 99(3–4), 421–430.
542 https://doi.org/10.1007/s00704-009-0152-7.
543 Kendall MG., &Gibbons JD. (1990). Rank Correlation Methods. Oxford University
544 Press: New York, NY, 272.
545 Kim, J. C., & Paik, K. (2015). Recent recovery of surface wind speed after decadal
546 decrease: a focus on South Korea. Clim. Dyn. 45(5–6), 1699–1712.
547 https://doi.org/10.1007/s00382-015-2546-9.
548 Kurosaki, Y., Shinoda, M., & Mikami, M. (2011). What caused a recent increase in

549 dust outbreaks over East Asia? Geophys. Res. Lett. 38(11), 1–6.
550 https://doi.org/10.1029/2011GL047494.
551 Lee, J. J., & Kim, C. H. (2012). Roles of surface wind, NDVI and snow cover in the
552 recent changes in Asian dust storm occurrence frequency. Atmos. Environ. 59(9),
553 366–375. https://doi.org/10.1016/j.atmosenv.2012.05.022.
554 Lin, C., Yang, K., Qin, J., & Fu, R. (2013). Observed coherent trends of surface and
555 upper-air wind speed over China since 1960. J. Clim. 26(9), 2891–2903.
556 https://doi.org/10.1175/JCLI-D-12-00093.1.
557 Lugato, E., Paustian, K., Panagos, P., Jones, A., & Borrelli, P. (2016). Quantifying the
558 erosion effect on current carbon budget of European agricultural soils at high
559 spatial resolution. Glob. Chang. Biol. 22(5), 1976–1984.
560 https://doi.org/10.1111/gcb.13198.
561 McVicar, T. R., Van Niel, T. G., Li, L. T., Roderick, M. L., Rayner, D. P., Ricciardulli,
562 L., & Donohue, R. J. (2008). Wind speed climatology and trends for Australia,
563 1975-2006: Capturing the stilling phenomenon and comparison with near-surface
564 reanalysis output. Geophys. Res. Lett. 35(20), 1–6.
565 https://doi.org/10.1029/2008GL035627.
566 Metternicht, G., Zinck, J. A., Blanco, P. D., & del Valle, H. F. (2010). Remote Sensing
567 of Land Degradation: Experiences from Latin America and the Caribbean. Journal
568 of Environmental Quality, 39, 42–61. https://doi.org/10.2134/jeq2009.0127.
569 McVicar, T. R., Roderick, M. L., Donohue, R. J., Li, L. T., Van Niel, T. G., Thomas,
570 A., … Dinpashoh, Y. (2012). Global review and synthesis of trends in observed
571 terrestrial near-surface wind speeds: Implications for evaporation. J. Hydrol.
572 416–417, 182–205. https://doi.org/10.1016/j.jhydrol.2011.10.024.
573 Mezősi, G., Blanka, V., Bata, T., Kovacs, F., & Meyer, B. (2015). Estimation of

574 regional differences in wind erosion sensitivity in Hungary. Nat. Hazards Earth
575 Syst. Sci. 15(1), 97–107. https://doi.org/10.5194/nhess-15-97-2015.
576 Miao, C. Y., Yang, L., Chen, X. H., & Gao, Y. (2012). The vegetation cover dynamics
577 (1982-2006) in different erosion regions of the Yellow River Basin, China. L.
578 Degrad. Dev. 23(1), 62–71. https://doi.org/10.1002/ldr.1050.
579 Munson, S. M., Belnap, J., & Okin, G. S. (2011). Responses of wind erosion to
580 climate-induced vegetation changes on the Colorado Plateau. Proc. Natl. Acad. Sci.
581 108(10), 3854–3859. https://doi.org/10.1073/pnas.1014947108.
582 MWRPRC (Ministry of Water Resources of the People's Republicof China). (2008).
583 Standards for Classification and Gradation of Soil Erosion (SL190–2007). Beijing:
584 Ministry of Water Resources of the People's Republic of China Press.
585 Pi, H., & Sharratt, B. (2017). Evaluation of the RWEQ and SWEEP in simulating soil
586 and PM10 loss from a portable wind tunnel. Soil Tillage Res. 170, 94–103.
587 https://doi.org/10.1016/j.still.2017.03.007.
588 Piao, S., Yin, G., Tan, J., Cheng, L., Huang, M., Li, Y., … Wang, Y. (2015). Detection
589 and attribution of vegetation greening trend in China over the last 30 years. Glob.
590 Chang. Biol. 21(4), 1601–1609. https://doi.org/10.1111/gcb.12795.
591 Pirazzoli, P. A., & Tomasin, A. (2003). Recent near-surface wind changes in the
592 central Mediterranean and Adriatic areas. Int. J. Climatol. 23(8), 963–973.
593 https://doi.org/10.1002/joc.925.
594 Reiche, M., Funk, R., Zhang, Z., Hoffmann, C., Reiche, J., Wehrhan, M., … Sommer,
595 M. (2012). Application of satellite remote sensing for mapping wind erosion risk
596 and dust emission-deposition in Inner Mongolia grassland, China. Grassland
597 Science, 58(1), 8–19. https://doi.org/10.1111/j.1744-697X.2011.00235.x.
598 Ren, S., Chen, X., Lang, W., & Schwartz, M. D. (2018). Climatic controls of the

599 spatial patterns of vegetation phenology in mid-latitude grasslands of the Northern
600 Hemisphere. J. Geophys. Res. Biogeosciences.
601 https://doi.org/10.1029/2018JG004616.
602 Riksen, M. J. P. M., & De Graaff, J. (2001). On-site and off-site effects of wind
603 erosion on European light soils. L. Degrad. Dev. 12(1), 1–11.
604 https://doi.org/10.1002/ldr.423.
605 Roderick, M. L., Rotstayn, L. D., Farquhar, G. D., & Hobbins, M. T. (2007). On the
606 attribution of changing pan evaporation. Geophys. Res. Lett. 34(17), 1–6.
607 https://doi.org/10.1029/2007GL031166.
608 Santra, P., Moharana, P. C., Kumar, M., Soni, M. L., Pandey, C. B., Chaudhari, S. K.,
609 & Sikka, A. K. (2017). Crop production and economic loss due to wind erosion in
610 hot arid ecosystem of India. Aeolian Research, 28, 71–82.
611 https://doi.org/https://doi.org/10.1016/j.aeolia.2017.07.009.
612 Segovia, C., Gómez, J. D., Gallardo, P., Lozano, F. J., & Asensio, C. (2017). Soil
613 nutrients losses by wind erosion in a citrus crop at southeast Spain. Eurasian Soil
614 Sci. 50(6), 756-763. https://doi.org/10.1134/S1064229317060114.
615 Shi, P. J., Sun, S., Wang, M., Li, N., Wang, J. A., Jin, Y. Y., … Yin, W. X. (2014).
616 Climate change regionalization in China (1961–2010). Sci. China Earth Sci.
617 57(11), 2676–2689. https://doi.org/10.1007/s11430-014-4889-1.
618 Shi, P. J., Zhang, G. F., Kong, F., & Ye, Q. (2015). Wind speed change regionalization
619 in China (1961-2012). Adv. Clim. Chang. Res. 6(2), 151–158.
620 https://doi.org/10.1016/j.accre.2015.09.006.
621 Shi, P., Zhang, G., Kong, F., Chen, D., Azorin-Molina, C., & Guijarro, J. A. (2019).
622 Variability of winter haze over the Beijing-Tianjin-Hebei region tied to wind
623 speed in the lower troposphere and particulate sources. Atmos. Res. 215, 1–11.

https://doi.org/10.1016/j.atmosres.2018.08.013.

Song, H., Zhang, K., Piao, S., & Wan, S. (2016). Spatial and temporal variations of spring dust emissions in northern China over the last 30 years. Atmos. Environ. 126, 117–127. https://doi.org/10.1016/j.atmosenv.2015.11.052.

Tegen, I., Lacis, A.A., Fung, I., 1996. The influence on climate forcing of mineral aerosols from disturbed soils. Nature. 380, 419–422.

Van Pelt, R. S., Zobeck, T. M., Potter, K. N., Stout, J. E., & Popham, T. W. (2004). Validation of the wind erosion stochastic simulator (WESS) and the revised wind erosion equation (RWEQ) for single events. Environ. Model. Softw. 19(2), 191–198. https://doi.org/10.1016/S1364-8152(03)00122-1.

Vautard, R., Cattiaux, J., Yiou, P., Thépaut, J. N., & Ciais, P. (2010). Northern Hemisphere atmospheric stilling partly attributed to an increase in surface roughness. Nat. Geosci. 3(11), 756–761. https://doi.org/10.1038/ngeo979.

Visser, S. M., Sterk, G., & Karssenberg, D. (2005). Wind erosion modelling in a Sahelian environment. Environ. Model. Softw. 20(1), 69–84. https://doi.org/10.1016/j.envsoft.2003.12.010.

Wan, H., Wang, X. L., & Swail, V. R. (2010). Homogenization and trend analysis of Canadian near-surface wind speeds. J. Clim. 23(5), 1209–1225. https://doi.org/10.1175/2009JCLI3200.1.

Wang, J., Xu, X., & Liu, P. (1999). Land use and land carrying capacity in ecotone between agriculture and animal husbandry in northern china.Resources Science. 21(5), 19-24. (in Chinese with an English abstract).

Wang, R., Liu, B., Li, H., Zou, X., Wang, J., Liu, W., … Zhang, C. (2017). Variation of strong dust storm events in Northern China during 1978–2007. Atmos. Res. 183, 166–172. https://doi.org/10.1016/j.atmosres.2016.09.002.

649 Wang, Y. Q., & Shao, M. A. (2013). Spatial variability of soil physical properties in a
650 region of the loess plateau of pr china subject to wind and water erosion. L.
651 Degrad. Dev. 24(3), 295–304. https://doi.org/10.1002/ldr.1128.
652 Xu, T., & Hutchinson, M. F. (2013). New developments and applications in the
653 ANUCLIM spatial climatic and bioclimatic modelling package. Environ. Model.
654 Softw. 40(July), 267–279. https://doi.org/10.1016/j.envsoft.2012.10.003.
655 Yan, Y., Xin, X., Xu, X., Wang, X., Yang, G., Yan, R., & Chen, B. (2013).
656 Quantitative effects of wind erosion on the soil texture and soil nutrients under
657 different vegetation coverage in a semiarid steppe of northern China. Plant and
658 Soil, 369(1), 585–598. https://doi.org/10.1007/s11104-013-1606-3.
659 Youssef, F., Visser, S., Karssenberg, D., Bruggeman, A., & Erpul, G. (2012).
660 Calibration of RWEQ in a patchy landscape; a first step towards a regional scale
661 wind erosion model. Aeolian Research, 3(4), 467–476.
662 https://doi.org/https://doi.org/10.1016/j.aeolia.2011.03.009.
663 Yue, Y., Shi, P., Zou, X., Ye, X., Zhu, A. xing, & Wang, J. ai. (2015). The
664 measurement of wind erosion through field survey and remote sensing: a case
665 study of the Mu Us Desert, China. Nat. Hazards. 76(3), 1497–1514.
666 https://doi.org/10.1007/s11069-014-1516-6.
667 Zhai, X., Huang, D., Tang, S., Li, S., Guo, J., Yang, Y., … Wang, K. (2017). The
668 emergy of metabolism in different ecosystems under the same environmental
669 conditions in the agro-pastoral ecotone of northern China. Ecological Indicators,
670 74, 198–204. https://doi.org/https://doi.org/10.1016/j.ecolind.2016.11.028.
671 Zhang, R., Arimoto, R., An, J., Yabuki, S., & Sun, J. (2005). Ground observations of a
672 strong dust storm in Beijing in March 2002. J. Geophys. Res. Atmos. 110(18), 1–8.
673 https://doi.org/10.1029/2004JD004589.

674 Zhang, C. L., Yang, S., Pan, X. H., & Zhang, J. Q. (2011). Estimation of farmland soil
675 wind erosion using RTK GPS measurements and the 137Cs technique: A case
676 study in Kangbao County, Hebei province, northern China. Soil Tillage
677 Res. 112(2), 140-148. https://doi.org/10.1016/j.still.2010.12.003.
678 Zhang, J. Q., Zhang, C. L., Chang, C. P., Wang, R. De, & Liu, G. (2017). Comparison
679 of wind erosion based on measurements and SWEEP simulation: A case study in
680 Kangbao County, Hebei Province, China. Soil Tillage Res. 165, 169–180.
681 https://doi.org/10.1016/j.still.2016.08.006.
682 Zhang, H., Fan, J., Cao, W., Harris, W., Li, Y., Chi, W., & Wang, S. (2018). Response
683 of wind erosion dynamics to climate change and human activity in Inner Mongolia,
684 China during 1990 to 2015. Sci. Total Environ. 639, 1038–1050.
685 https://doi.org/10.1016/j.scitotenv.2018.05.082.
686 Zhao, H. L., Yi, X. Y., Zhou, R. L., Zhao, X. Y., Zhang, T. H., & Drake, S. (2006).
687 Wind erosion and sand accumulation effects on soil properties in Horqin Sandy
688 Farmland, Inner Mongolia. Catena. 65(1), 71–79.
689 https://doi.org/10.1016/j.catena.2005.10.001.
690 Zhao, Y., Wu, J., He, C., & Ding, G. (2017). Linking wind erosion to ecosystem
691 services in drylands: a landscape ecological approach. Landsc. Ecol. 32(12),
692 2399–2417. https://doi.org/10.1007/s10980-017-0585-9.
693 Zhou, Y., Guo, B., Wang, S., & Tao, H. (2015). An estimation method of soil wind
694 erosion in Inner Mongolia of China based on geographic information system and
695 remote sensing. J. Arid Land. 7(3), 304–317.
696 https://doi.org/10.1007/s40333-015-0122-0
697 Zhou, X., Yamaguchi, Y., & Arjasakusuma, S. (2018). Distinguishing the vegetation
698 dynamics induced by anthropogenic factors using vegetation optical depth and

AVHRR NDVI: A cross-border study on the Mongolian Plateau. Sci. Total Environ. 616–617, 730–743. https://doi.org/10.1016/j.scitotenv.2017.10.253.

Zhuang, G., Guo, J., Yuan, H., & Zhao, C. (2001). The compositions, sources, and size distribution of the dust storm from China in spring of 2000 and its impact on the global environment. Chinese Sci. Bull. 46(11), 895–900. https://doi.org/10.1007/BF02900460.

Zou, X. K., & Zhai, P. M. (2004). Relationship between vegetation coverage and spring dust storms over northern China. J. Geophys. Res. Atmos. 109(D3), https://doi.org/10.1029/2003JD003913.

711 **Table captions**

712 Table 1. Data required for the wind erosion model RWEQ and the assessment of climate variability. Note: 'N/A' means not applicable.

Data types	Temporal resolution	Spatial resolution	Time period	Data source
Wind speed	3-hour	N/A	1982-2016	National Oceanic and Atmospheric Administration of the United States (NOAA, http://cdc.cma.gov.cn/; last accessed 1 November 2018)
Soil moisture	Daily	0.25º latitude x longitude	1982-2016	European Space Agency (ESA, http://www.esa-soilmoisture-cci.org/; last accessed 1 November 2018)
Snow depth	Daily	25km	1982-2016	Western China Environmental and Ecological Science Data Center (WCEEC, http://westdc.westgis.ac.cn/; last accessed 1 November 2018)
Fractional vegetation cover	Daily	1km	1999-2016	Copernicus Global Land Service (CGLS,https://land.copernicus.eu/global/; last accessed 1 November 2018)
Normalized Difference Vegetation Index	Daily	8km	1982-2006	Environmental and Ecological Science Data Center for West China (http://westdc.westgis.ac.cn/data/; last accessed 1 November 2018)
Air temperature	Daily	0.5º latitude x longitude	1982-2016	Climatic Research Unit of the University of East Anglia (CRU,http://www.cru.uea.ac.uk/; last accessed 1 November 2018)
Dust storm frequency	Daily	N/A	1982-2007	China Meteorological Administration (CMA,http://data.cma.cn/; last accessed 1 November 2018)

Precipitation	Daily	0.5º latitude x longitude	1982-2016	China Meteorological Administration (CMA,http://data.cma.cn/; last accessed 1 November 2018)

Table 2. Area (in km^2) and proportion (in %) of annual and seasonal SLWE (in t ha^{-2}) across EANC from1982 to 2016.

Wind erosion intensity	SLWE	Annual		Winter		Spring		Summer		Autumn	
		Area	Proportion	Area	Proportion	Area	Proportion	Area	Proportion	Area	Proportion
mired	0 - 2	0.9	1.7	7.21	13.4	0.94	1.7	12.3	22.9	2.63	4.9
mild	2 - 25	4.52	8.4	30.79	57.4	10.67	19.9	30.13	56.2	36.98	68.9
moderate	25 - 50	11.88	22.1	9.99	18.6	14.12	26.3	6.68	12.4	9.17	17.1
strong	50 - 80	8.42	15.7	3.57	6.7	8.99	16.8	2.28	4.2	2.29	4.3
very strong	80 -150	10.93	20.4	2.03	3.8	10.77	20.1	1.34	2.5	0.86	1.6
fierce	> 150	17	31.7	0.04	0.1	8.17	15.2	0.92	1.7	1.72	3.2

Table 3. Relative percentage (in %) of areas with significant (at $p<0.05$ and $p<0.10$) and non-significant (at $p>0.10$) negative and positive trends of annual and seasonal SLWE across EANCfrom1982 to 2016.

	Positive	Positive $p<0.05$	Positive $p<0.10$	Positive $p>0.10$	Negative	Negative $p<0.05$	Negative $p<0.10$	Negative $p>0.10$
Annual	0.0	0.0	0.0	0.0	100	99.8	99.9	0.1
Winter	3.8	3.2	6.7	93.3	96.2	86.6	89.4	10.6
Spring	0.1	0.0	0.0	100	99.9	98.9	99.2	0.8
Summer	0.6	4.0	11.9	88.1	99.4	95.9	96.9	3.1
Autumn	0.0	0.0	0.0	0.0	100	100	100	0.0

Supplementary materials

Table S1 Description of meteorological stations in the EANC and surrounding areas.

Number	Station	Latitude (°N)	Longitude (°E)	Elevation (m.a.s.l.)	Area	Location of stations
1	Huma	51.72	126.65	178	Heilongjiang	Plain
2	Heihe	50.25	127.45	167	Heilongjiang	Plain
3	Hailar	49.22	119.75	613	Inner Mongolia	Mountain
4	Xiaoergou	49.20	123.72	287	Mongolia	Mountain
5	Nenjiang	49.17	125.23	243	Heilongjiang	Plain
6	Sunwu	49.43	127.35	235	Heilongjiang	Plain
7	Borktu	48.77	121.92	742	Inner Mongolia	Mountain
8	Keshan	48.05	125.88	236	Heilongjiang	Plain
9	Oer mountain	47.17	119.95	1028	Inner Mongolia	Mountain
10	Qiqihar	47.38	123.92	147	Heilongjiang	Plain
11	Helen	47.43	126.97	240	Heilongjiang	Plain
12	Yichun	47.73	128.92	246	Heilongjiang	Mountain
13	Fujin	47.23	131.98	65	Heilongjiang	Plain
14	Tailai	46.40	123.42	151	Heilongjiang	Plain
15	Anda	46.38	125.32	150	Heilongjiang	Plain
16	Baoqing	46.32	132.18	84	Heilongjiang	Plain
17	East Wuzhumu	45.52	116.97	840	Inner Mongolia	Mountain
18	The former Guoerluo	45.12	124.83	138	Jilin	Plain
19	Harbin	45.75	126.77	143	Heilongjiang	Plain
20	Tong river	45.97	128.73	110	Heilongjiang	Plain
21	Fashion view	45.22	127.97	191	Heilongjiang	Plain
22	Jixi	45.28	130.95	238	Heilongjiang	Plain
23	O ba ga flag	44.02	114.95	1128	Inner Mongolia	Plateau
24	Zhu Ri and	42.40	112.90	1152	Inner Mongolia	Plateau
25	Middle Wulate	41.57	108.52	1290	Inner Mongolia	Plateau
26	Daerhanmao	41.70	110.43	1377	Inner Mongolia	Plateau
27	Huade	41.90	114.00	1485	Inner Mongolia	Plateau
28	Hohhot	40.82	111.68	1065	Inner Mongolia	Plateau
29	Jining	41.03	113.07	1422	Mongolia	Plateau
30	Datong	40.10	113.33	1069	Shanxi	Plateau
31	Otog Banne	39.10	107.98	1381	Inner	Plateau

					Mongolia	
32	Dongsheng	39.83	109.98	1459	Inner Mongolia	Plateau
33	Hequ	39.38	111.15	862	Shanxi	Mountain
34	Wutai mountain	39.03	113.53	2898	Shanxi	Mountain
35	Yu county	39.83	114.57	910	hebei	Mountain
36	Yulin	38.23	109.70	1059	Shaanxi	Mountain
37	Yuamping	38.73	112.72	828	Shaanxi	Mountain
38	Shijiazhuang	38.03	114.42	81	Hebei	Plain
39	Lishi	37.50	111.10	951	Shanxi	Mountain
40	Taiyuan	37.78	112.55	780	Shanxi	Mountain
41	Jiexiu	37.03	111.92	746	Shanxi	Mountain
42	West wuzhumu	44.58	117.60	997	Inner Mongolia	Mountain
43	Jarud Banne	44.57	120.90	266	Inner Mongolia	Plain
44	Bahrain left Banne	43.98	119.40	486	Inner Mongolia	Mountain
45	Changling	44.25	123.97	190	Jilin	Plain
46	Mudanjiang	44.57	129.60	243	Heilongjiang	Plain
47	Xilinhaote	43.95	116.07	991	Inner Mongolia	Plateau
48	Linxi	43.60	118.07	800	Inner Mongolia	Plateau
49	Kailu	43.60	121.28	242	Inner Mongolia	Plain
50	Siping	43.18	124.33	165	Jilin	Plain
51	Changchun	43.90	125.22	239	Jilin	Plain
52	Dunhua	43.37	128.20	526	Jilin	Plain
53	Doren	42.18	116.47	1247	Inner Mongolia	Plateau
54	Chifeng	42.27	118.97	568	Inner Mongolia	Plateau
55	Baoguotu	42.33	120.70	402	Inner Mongolia	Montain
56	Zhangwu	42.42	122.53	84	Liaoning	Plain
57	Qingyuan	42.10	124.92	235	Liaoning	Montain
58	Fengning	41.22	116.63	661	Hebei	Montain
59	Weichang	41.93	117.75	844	Hebei	Montain
60	Chaoyang	41.55	120.45	176	Liaoning	Plain
61	Jinzhou	41.13	121.12	70	Liaoning	Coastal
62	Shenyang	41.20	123.07	45	Liaoning	Plain
63	Zhangjiakou	40.78	114.88	726	Hebei	Montain
64	Huailai	40.40	115.50	542	Hebei	Montain
65	Chengde	40.97	117.93	374	Hebei	Montain
66	Tsing lung	40.40	118.95	229	Hebei	Plain
67	Beijing	39.80	116.47	32	Beijing	Plain
68	Tianjin	39.08	117.07	4	Tianjin	Plain
69	Tangshan	39.67	118.15	29	Hebei	Plain

70	Leting	39.42	118.90	12	Hebei	Coastal
71	Baoding	38.85	115.52	19	Hebei	Plain

739

740

741 The full description of the RWEQ formulation.

742 I. Meteorological factor

743 The meteorological factor (MF) synthetically reflects the influence of various
744 meteorological factors on wind erosion. It is expressed as follows:

745 $$\mathrm{MF} = W_f * \frac{\rho}{g} * SW * SD \quad (1)$$

746 where, W_f is the wind factor（in $m^3\ s^{-3}$）; ρ is air density (in kg m^{-3}); g is the
747 acceleration of gravity (in m s^{-2}); *SW* is the soil moisture factor (dimensionless); *SD* is
748 the snow cover factor (dimensionless).

749 ① Wind factor

750 The wind factor (W_f) is shown in Eq.2:

751 $$W_f = \frac{\sum_{i=1}^{N} U_2(U_2-U_t)^2}{N} * N_d \quad (2)$$

752 where, U_2 is the wind speed at 2 m, and the wind profile (Karnauskas et al., 2018) was
753 used to convert wind speed at 10m to 2m ; U_t is the wind speed threshold, generally
754 set as 5 m s^{-1}; N_d is the time intervals for wind speed measures, usually about 15 days;
755 and, *N* is for wind speed observation frequency.

756 ② Soil moisture factor

757 The soil moisture factor (SW_f) is shown in Eq.3:

758 $$SW_f = 1 - SW \quad (3)$$

759 where, *SW* is soil moisture content (0-1).

760 ③ Snow cover factor

The snow cover factor (SD) is shown in Eq.4:

$$\mathrm{SD} = 1 - \mathrm{P}(\text{snow depth} > 25.4mm) \quad (4)$$

where, *P* (Snow depth> 25.4mm) is the probability that the snow cover depth is greater than 25.4mm in the calculation interval (15 days).

II. Soil erodibility factor

The value of the soil erodibility factor (EF) is calculated by Eq.5. (Fryrear et al., 2000). The actual calculation supposes that the soil erodibility of EANC remains unchanged during the period.

$$EF = \frac{29.09+0.31Sa+0.17Si+\frac{0.33Sa}{cl}-2.59OM-0.95CaCO_3}{100} \quad (5)$$

where, *Sa* is the sand grain proportion in the soil (5.5%~93.6%); *Si* is the proportion of soil silt (0.5%~69.5%); Sa/Cl is the ratio of soil sand grain and clay (1.2%~53.0%); *Cl* is proportion of clay (5.0%~39.3%); and $CaCO_3$ is proportion of calcium carbonate (0~25.2%). The data in brackets are the range required by the RWEQ.

III. Soil crust factor

The soil crust factor (SCF) infers to a layer of special characters on the soil surface, by the agglutination of soil particles (especially clay, silty, and organic matter) as shown in Eq. 6:

$$\mathrm{SCF} = \frac{1}{1+0.0066(\mathrm{cl})^2+0.021(\mathrm{OM})^2} \quad (6)$$

where, *cl* is proportion of clay (5.0%~39.3%) and OM is proportion of organic matter (0.32%~4.74%). The data in brackets are the range required by the RWEQ model.

IV. Surface roughness factor

In the RWEQ model, the surface roughness factor (K'), including random

roughness (Crr) and soil roughness (Kr), is calculated as Eq.7:

$$K' = e^{(1.86k_r - 2.41K_r^{-0.934} - 0.127Crr)} \quad (7)$$

On a regional scale, the random roughness (Crr) of farming produce was difficult to estimate. Therefore, soil roughness (Kr) is used instead of topographic roughness, calculated by the Smith-Carson equation (Li et al., 2006, Mendez et al., 2010) as shown in Eq.8:

$$K_r = 0.2 * \frac{\Delta(H)^2}{L} \quad (8)$$

where, Kr is topographic roughness (cm); Crr is the random roughness factor (cm), as 0 in the real calculation; K' is the terrain roughness factor (cm); L is the topographic fluctuate parameters; and ΔH is the difference of elevation above sea level for the distance L, the Neighborhood Statistics tool in GIS software was used to calculate the difference between adjacent cells of DEM data.

V. Vegetation cover factor

The vegetation cover factor is shown in Eq.9:

$$C = e^{-0.0438FVC} \quad (9)$$

where, FVC is fractional vegetation cover (in %).

References

Karnauskas, K. B., Lundquist, J. K., & Zhang, L. (2018). Southward shift of the global wind energy resource under high carbon dioxide emissions. Nature Geoscience, 11(1), 38–43. https://doi.org/10.1038/s41561-017-0029-9

Fryrear, D. W., Bilbro, J. D., Saleh, A., Schomberg, H., Stout, J. E., & Zobeck, T. M. (2000). RWEQ: Improved wind erosion technology. J. Soil Water Conserv. 55(2),

183–189.

Li, J., You, S., Huang, J. (2006). Spatial Distribution of Ground Roughness Length Based on GIS in China. Journal of Shanghai Jiaotong University (Agricultural Science). 24(2): 185-189. (In Chinese).

Mendez, M. J., & Buschiazzo, D. E. (2010). Wind erosion risk in agricultural soils under different tillage systems in the semiarid Pampas of Argentina. Soil Tillage Res. 106(2), 311–316. https://doi.org/10.1016/j.still.2009.10.010.

Figure

Figures

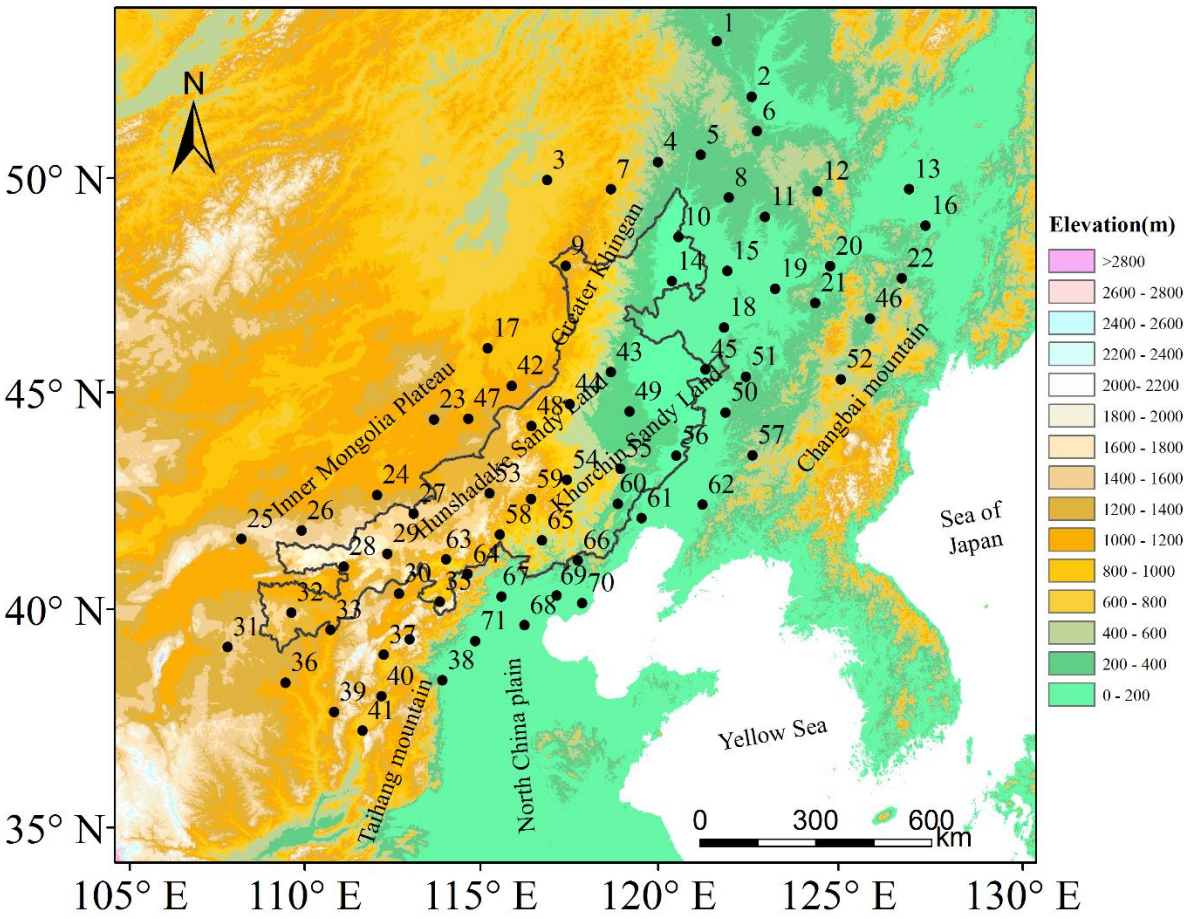

Figure 1. Terrain map of the EANC (black solid line area) showing the complex topography and location (for numbers and characteristics see Table S1) of the 71 homogenized stations for wind speed interpolation.

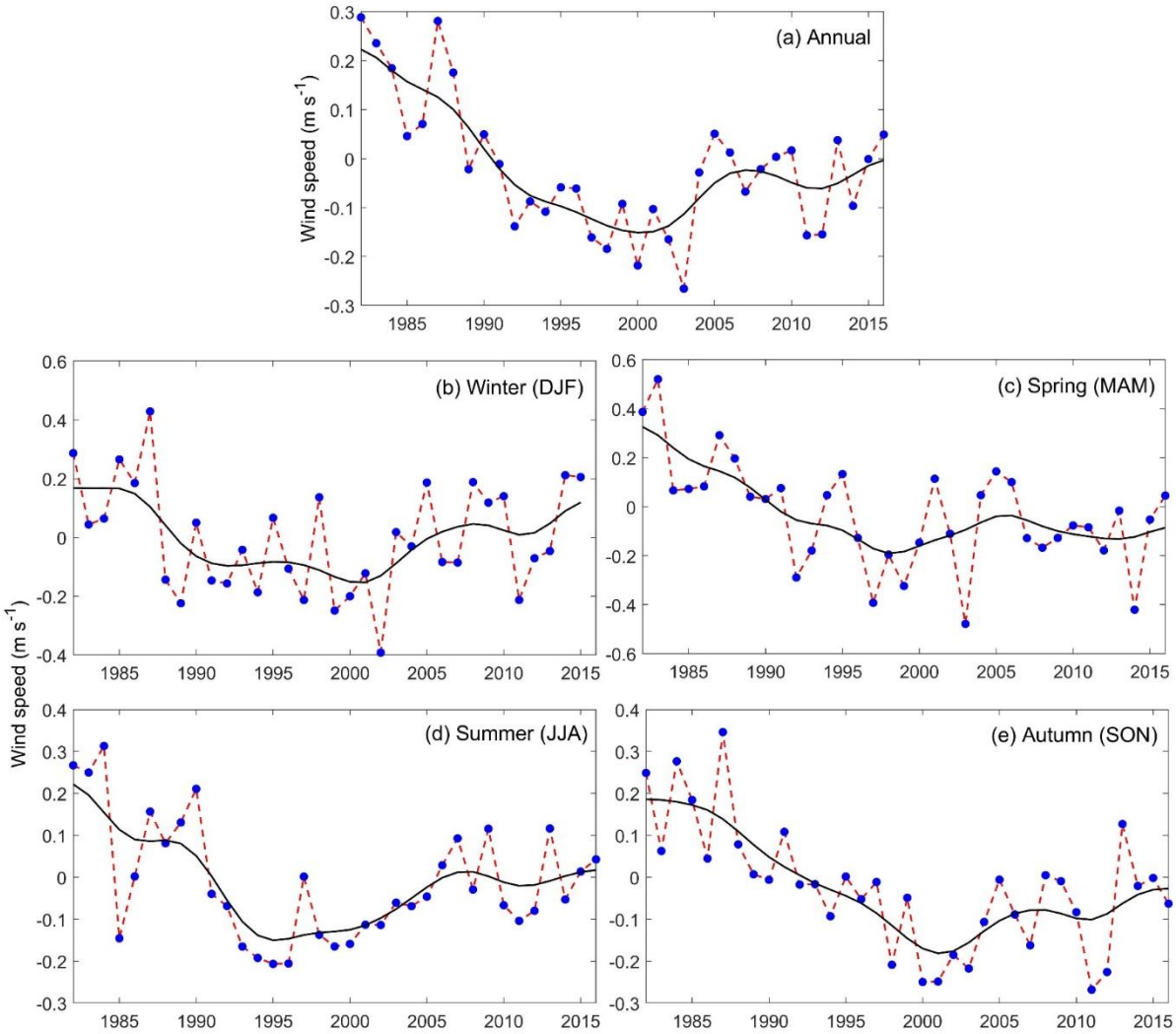

Figure 2. Annual and seasonal average wind speed anomaly across EANC from 1982 to 2016. The 11-year Gaussian low-pass filter is shown with a solid black line.

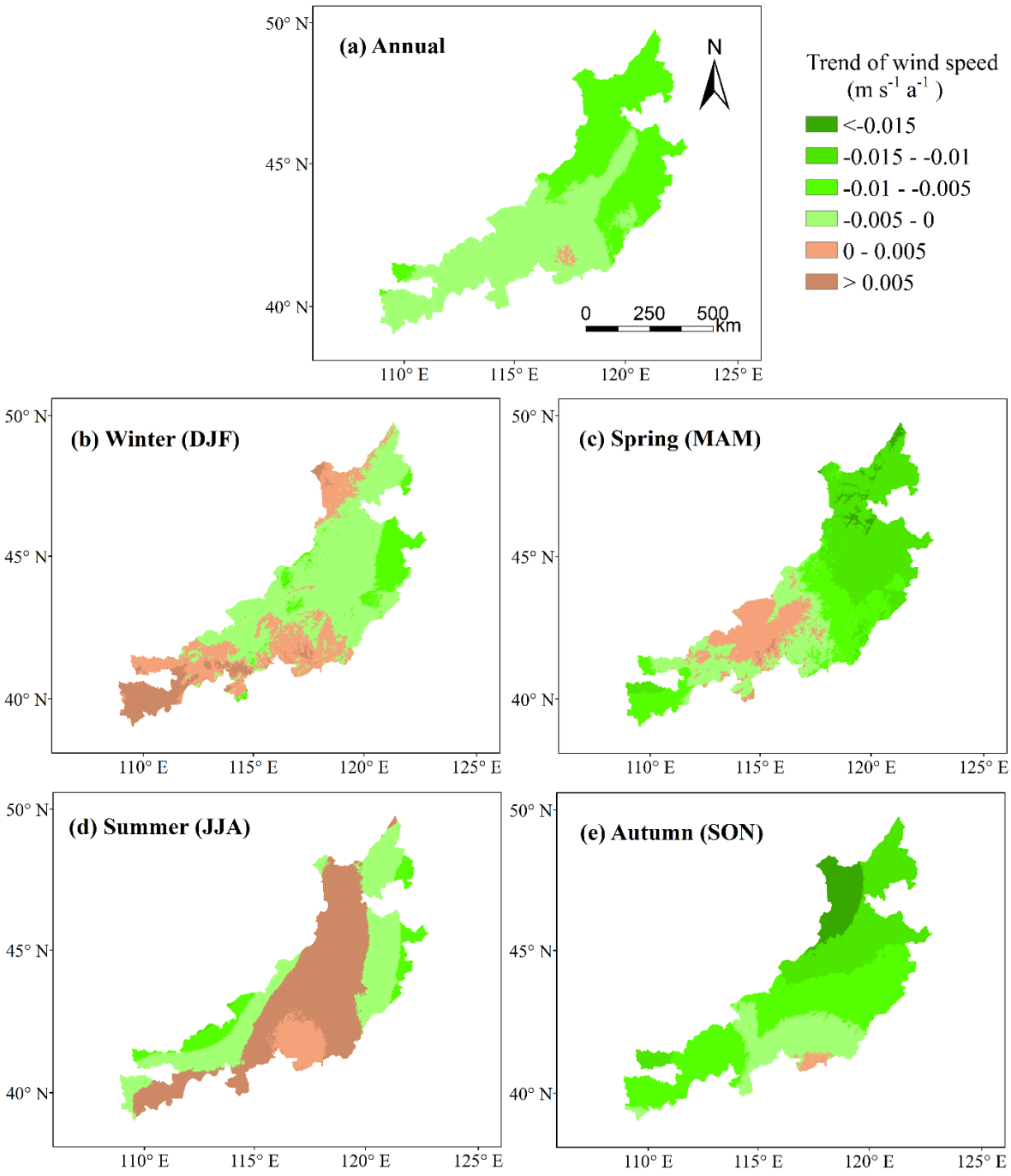

Figure 3. Annual and seasonal spatial distribution of wind speed trends across EANC from 1982 to 2016.

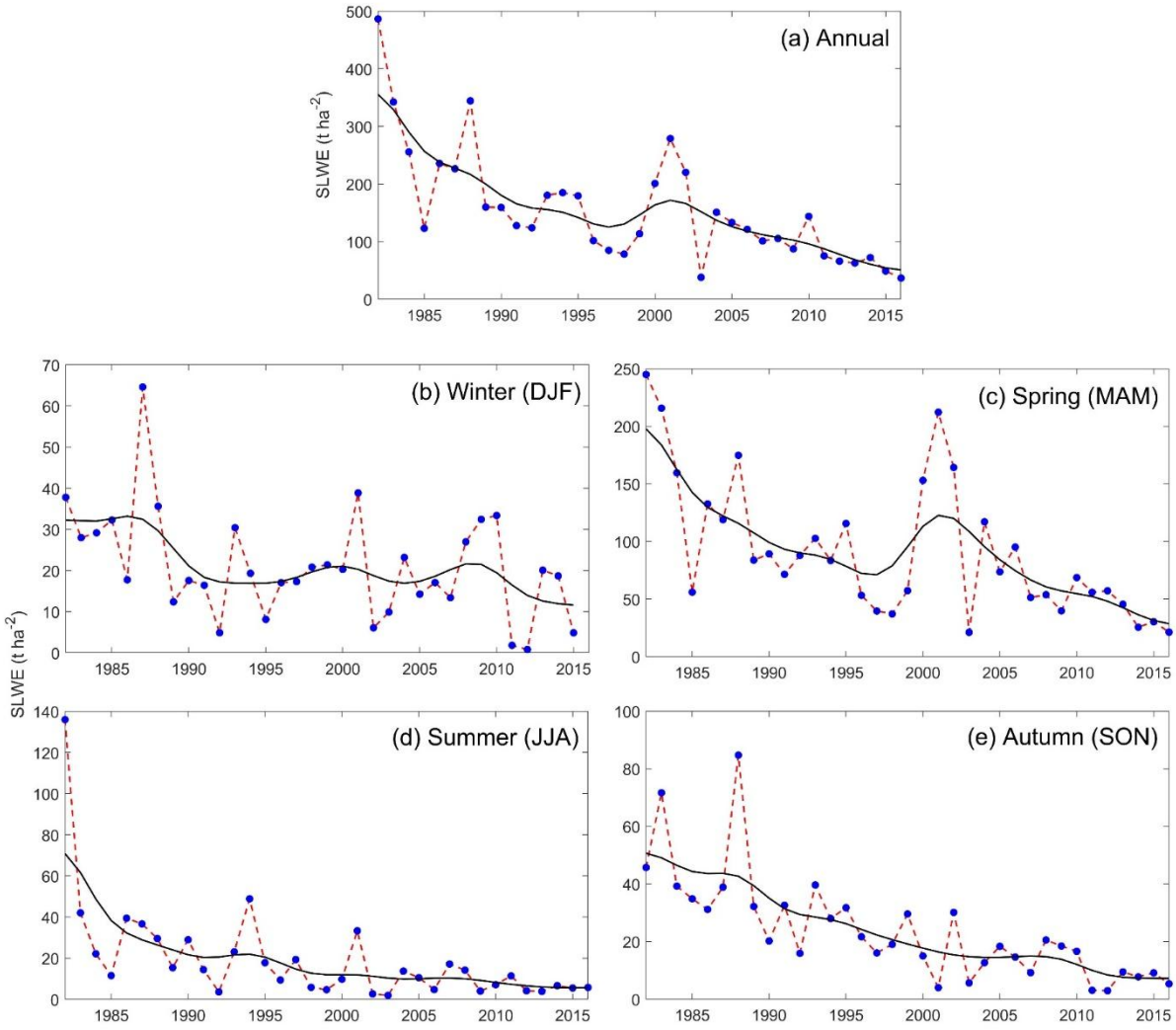

Figure 4. Annual and seasonal variability of SLWE across EANC from 1982 to 2016. The 11-year Gaussian low-pass filter is shown with a solid black line.

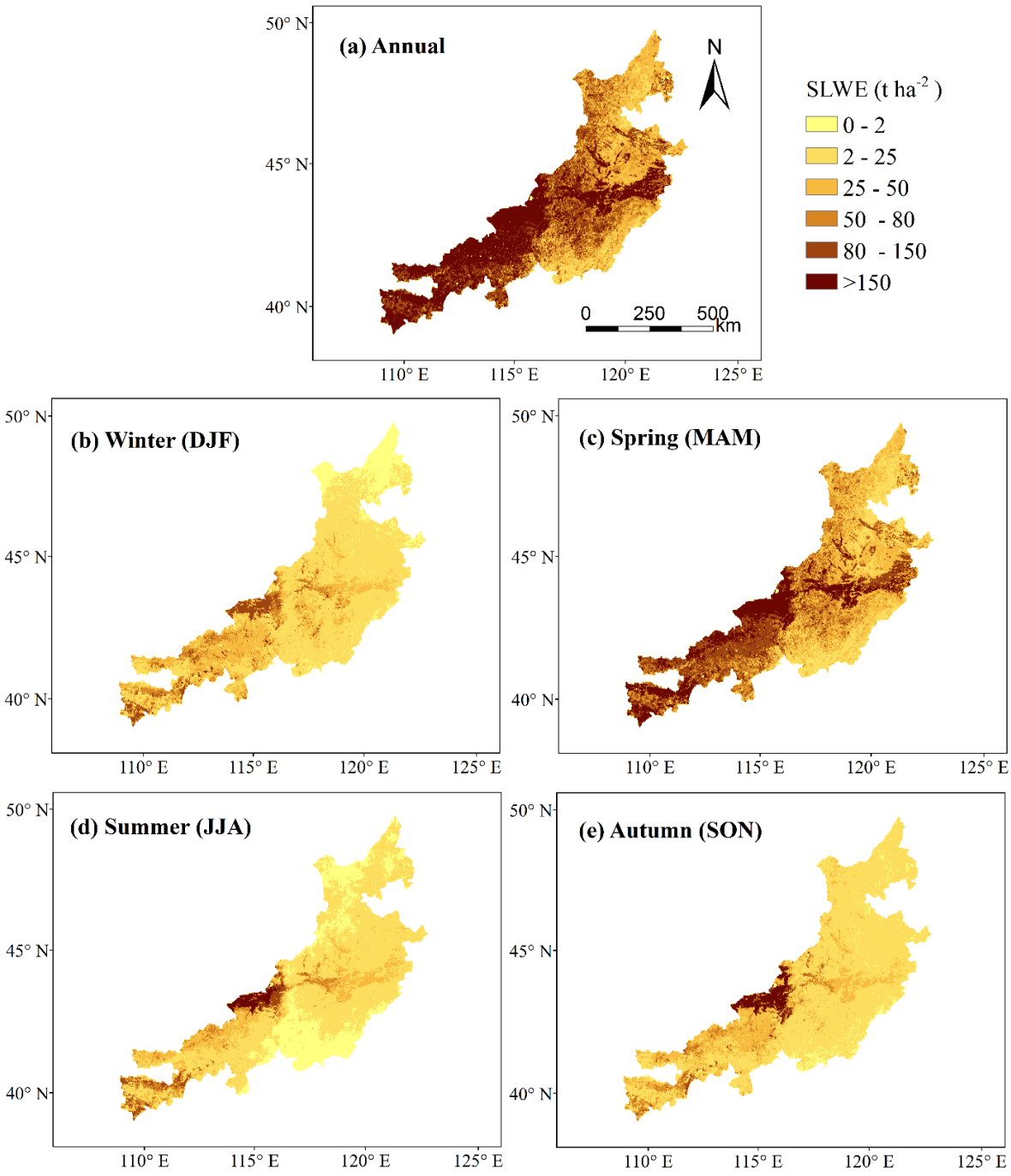

Figure 5. Spatial distribution of annual and seasonal SLWE across EANC for 1982 to 2016. The yellow to brown color indicate the different wind erosion intensity varied from mild to fierce.

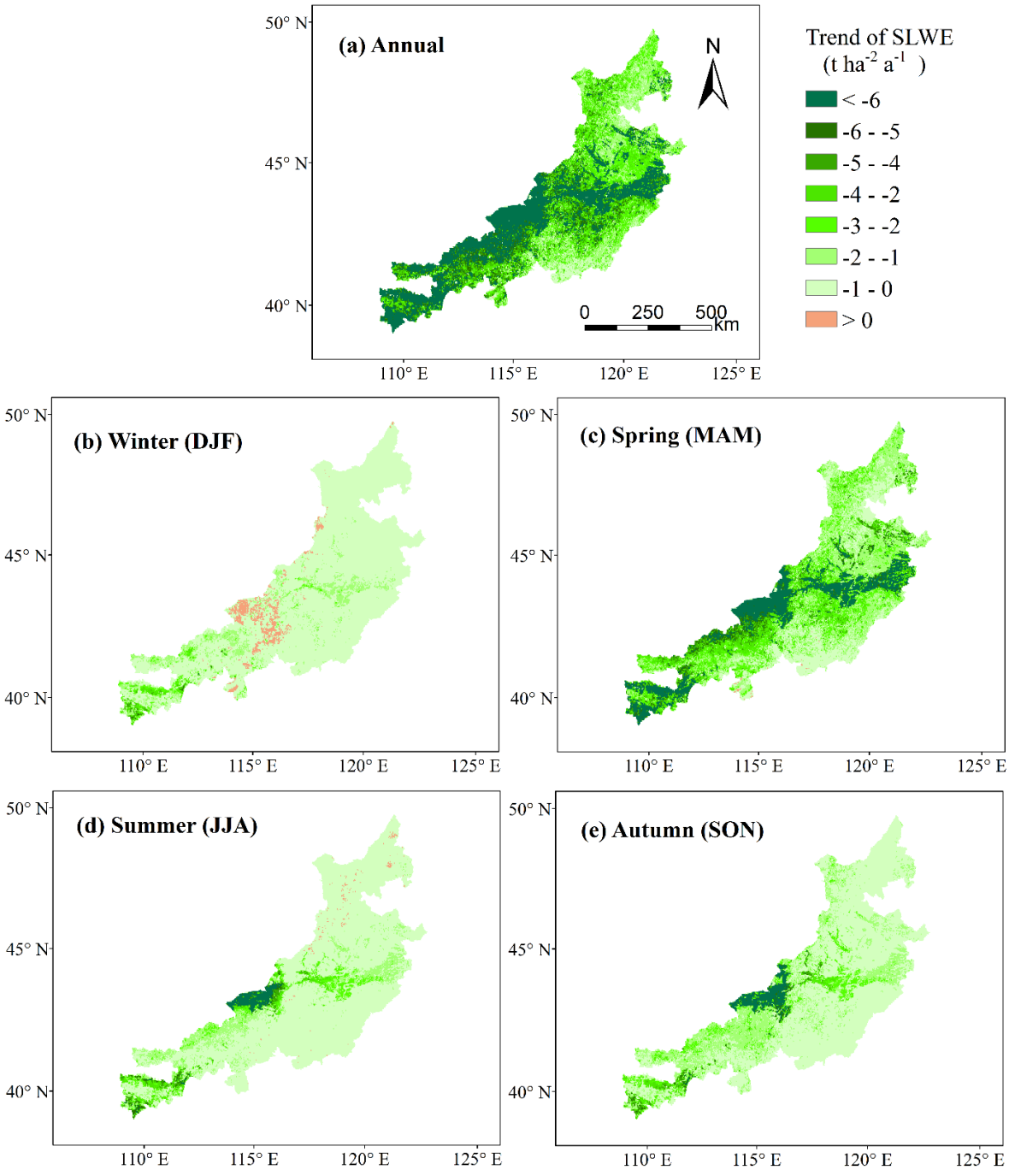

Figure 6. Spatial distribution of annual and seasonal trends of SLWE across EANC from 1982 to 2016.

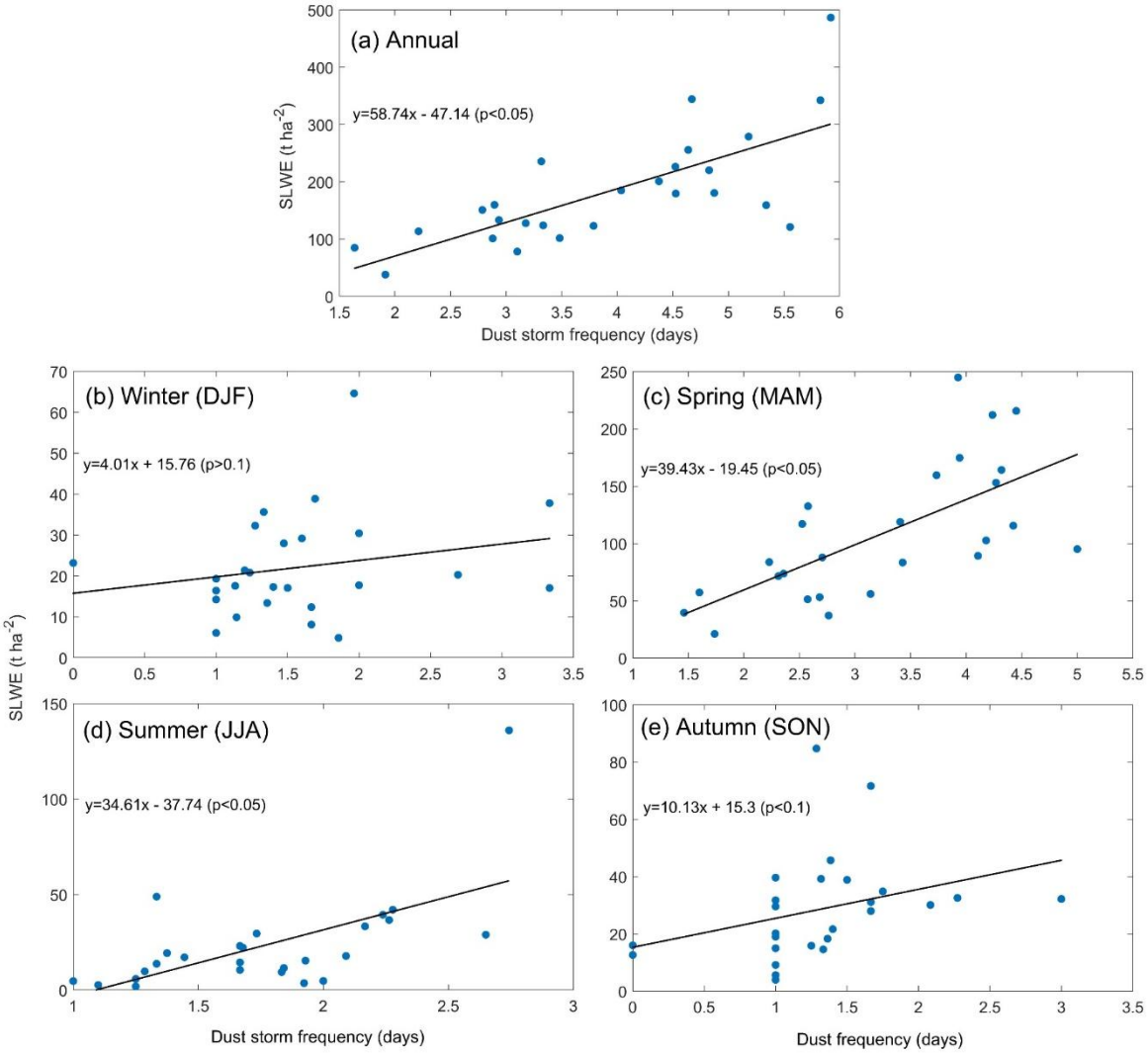

Figure 7. Annual and seasonal relationship between SLWE and dust storm frequency across EANC from 1982 to 2007. The linear regression model and fitted curve between SLWE and dust storm frequency also displayed in each plot.

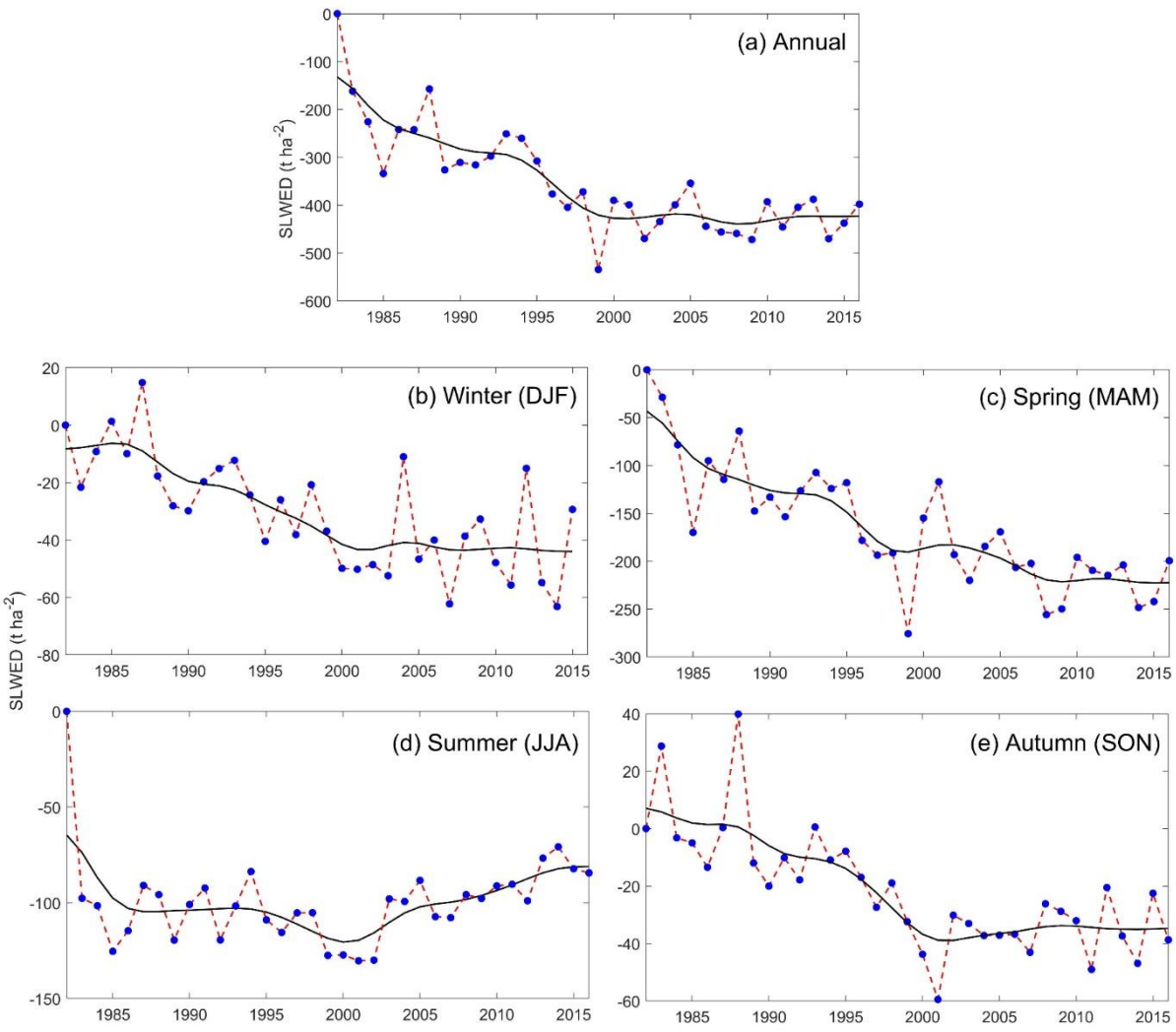

Figure 8. Annual and seasonal SLWED across EANC from 1982 to 2016. The 11-year Gaussian low-pass filter is shown with a solid black line.

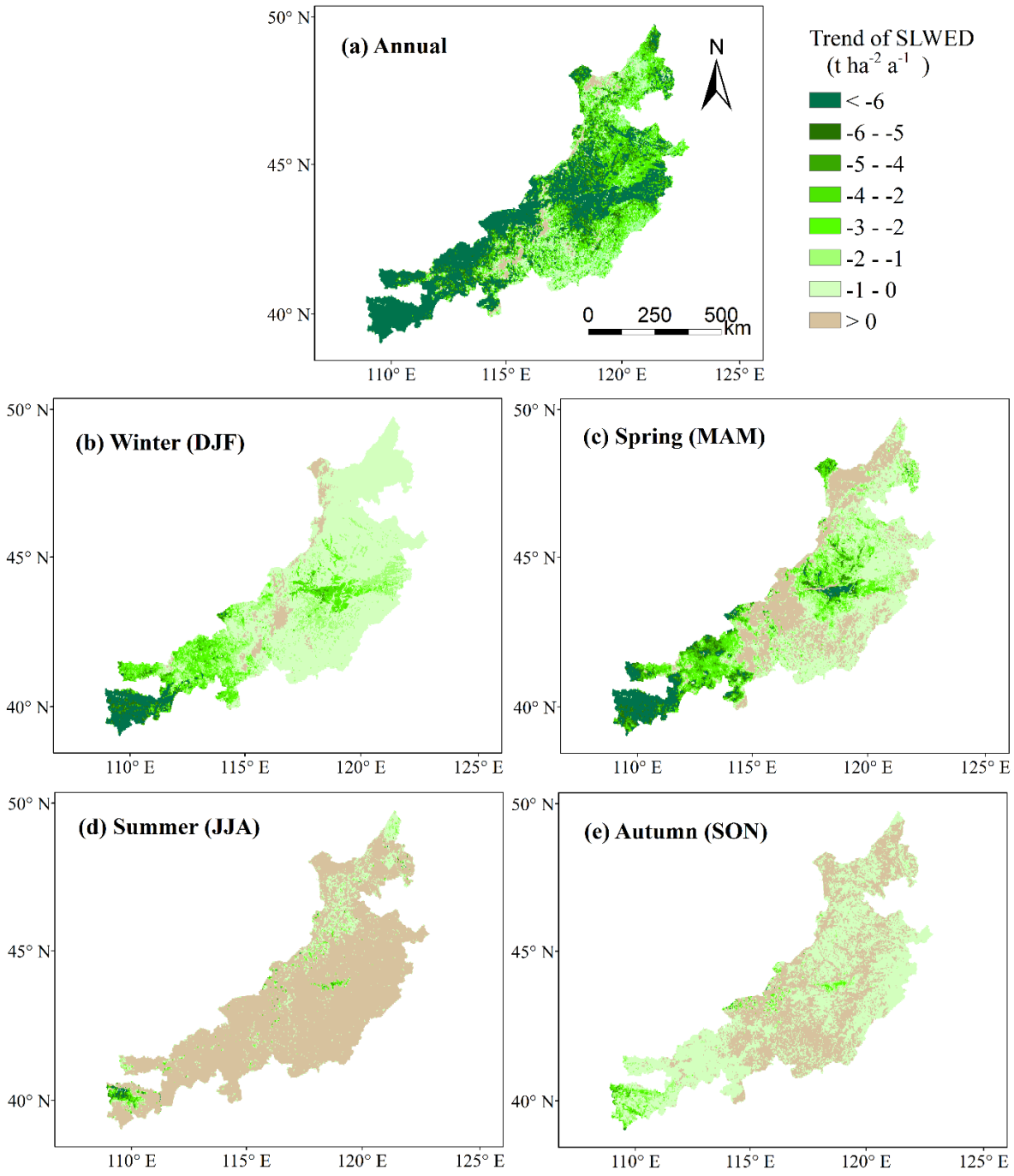

Figure 9. Spatial distribution of annual and seasonal SLWED across EANC from 1982 to 2016.

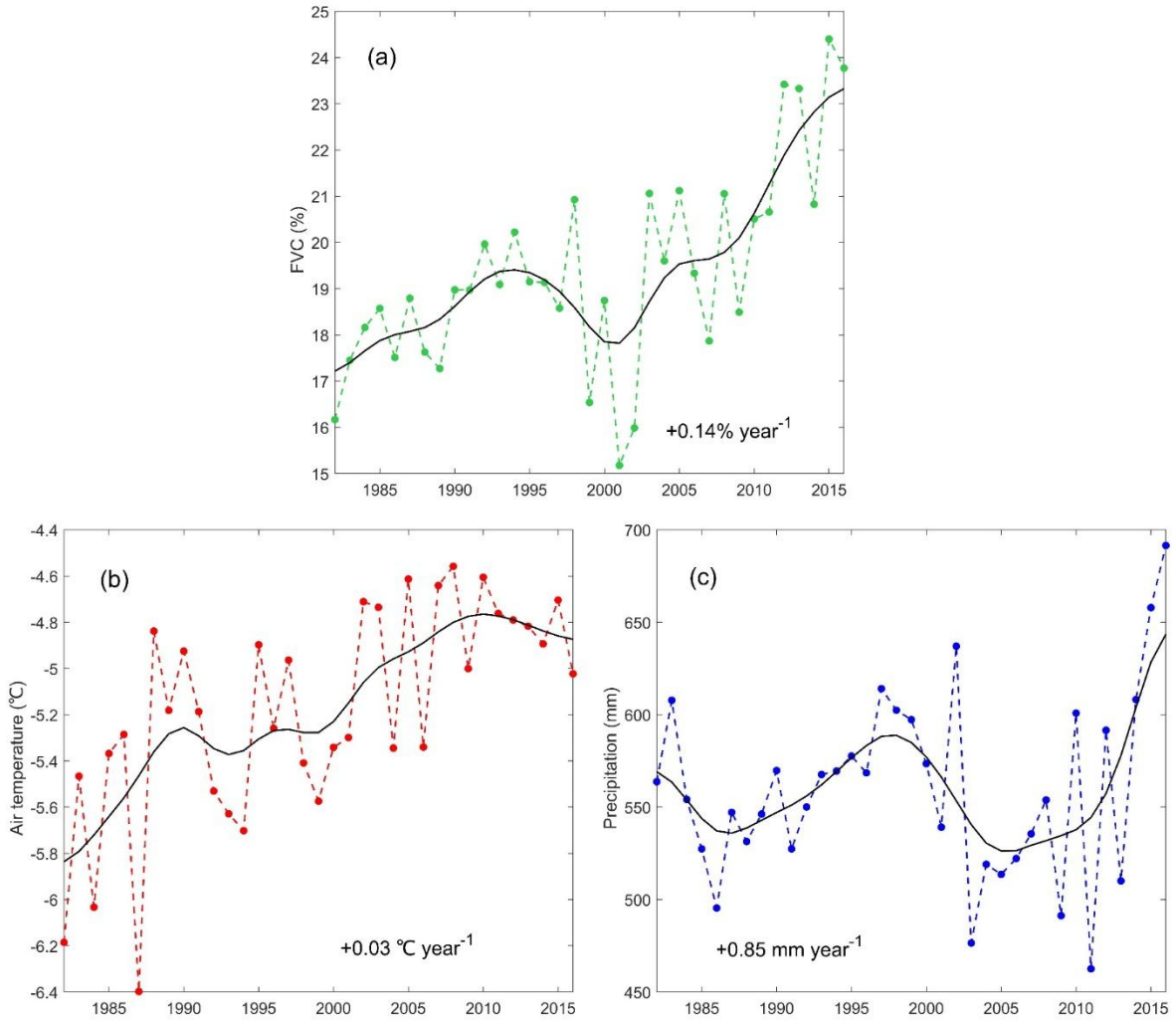

Figure 10. Temporal evolution of annual FVC (a), air temperature (b) and precipitation (c) across EANC from 1982 to 2016. The 11-year Gaussian low-pass filter is shown with a solid black line.